



Impact of B-site Substitution of Transition Metal (Fe and Mn) on the Structural, Electrical, and Magnetic Properties of Tungsten Bronze Ferroelectric Ceramic

Shristi Chaudhary¹ · Sheela Devi² · Shilpi Jindal¹ · Kamal Kumar Kushwah³

Received: 27 December 2023 / Accepted: 27 March 2024 / Published online: 30 April 2024
© The Minerals, Metals & Materials Society 2024

Abstract

The solid-state reaction approach was used to synthesize $\text{Ba}_{0.95}\text{Sr}_{0.05}\text{Ca}_5\text{Ti}_{2-x}\text{M}_x\text{Nb}_8\text{O}_{30}$ (where M represents Fe and Mn and x is 0 and 0.05) in order to compare the variations in the structural and dielectric properties of the ferroelectric material. The structural investigation was carried out using x-ray diffraction (XRD) and Fourier transform infrared (FTIR) spectroscopy. The orthorhombic structure with Pbcn space group revealed by the XRD investigation was validated by Rietveld refinement. The FTIR spectroscopy results were in good agreement with the reported phase. Analysis of the electrical properties was carried out by complex impedance spectroscopy. The results of transition metal doping with both Fe and Mn with regard to the dielectric permittivity as a function of frequency showed an improvement in the dielectric characteristics, while Mn exhibited a higher dielectric constant than Fe. The pure sample showed a lower transition temperature than the Fe- and Mn-doped sample. Analysis of the magnetic characteristics obtained from vibrating-sample magnetometry (VSM) revealed that doping enhanced the magnetic properties. This approach thus shows excellent potential for high-temperature operation, achieving good temperature stability via transition metal doping.

Keywords Ferroelectrics · tungsten bronze · dielectric · impedance spectroscopy

Introduction

With recent technological advancements, lead-free materials are increasingly crucial in electronics because lead-based materials are hazardous and harmful for the environment. The electrical and magnetic properties of lead-free materials are thus improved in order to expand their application potential. Tungsten bronze ferroelectric materials are currently being explored as a possible replacement for lead-based materials. Due to their exceptional electrical and magnetic properties for a variety of applications in electronics and

energy conversion such as perovskite, tungsten bronze ferroelectrics have received considerable attention. The typical formula for tungsten bronze is $[(A1)_2(A2)_4(C)_4][(B1)_2(B2)_8]O_{30}$, where C is smaller in size and is left empty, resulting in $A_6B_{10}O_{30}$. The pentagonal A_2 and square A_1 sites can obtain small cations Ba^{2+} , Sr^{2+} , and Ca^{2+} , and B_1 and B_2 octahedral sites are occupied by highly charged ions, Ti^{4+} , Nb^{5+} , Zn^{2+} .^{1–4}

Zhu et al. recently presented a detailed analysis on the ferroelectric transition and low-temperature dielectric relaxations in occupied tungsten bronze ceramics combined with probable multiferroicity.⁵ In-depth studies have been conducted on the ferroelectric properties of $M_4R_2Ti_4Nb_6O_{30}$ and $M_5RTi_3Nb_7O_{30}$ tungsten bronzes.^{6–12} It is thought that structural modulation caused by oxygen octahedral tilting predominantly determines the type of phase transition and transition temperature. However, a variety of niobates (e.g., $\text{Ba}_5\text{RTi}_3\text{Nb}_7\text{O}_{30}$, $\text{Ba}_3\text{R}_3\text{Ti}_5\text{Nb}_5\text{O}_{30}$, and $\text{Ba}_4\text{R}_2\text{Ti}_4\text{Nb}_6\text{O}_{30}$ of $\text{BaO-R}_2\text{O}_3\text{-TiO}_2\text{-Nb}_2\text{O}_5$ [R = Dy, La, Nd, Sm, and Y] systems) and vanadates (e.g., $\text{NaBa}_{2x}\text{O}_{15}$ [x = Nb and Ta] and

✉ Sheela Devi
physics.sheela@gmail.com

¹ Chandigarh University, Gharuan, Mohali, Punjab 140413, India

² Maharaja Surajmal Institute of Technology, Janakpuri, New Delhi, Delhi 110058, India

³ Department of Applied Physics, Jabalpur Engineering College, Jabalpur, Madhya Pradesh, India

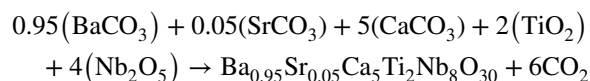
$\text{Ba}_2\text{Pb}_2\text{Sm}_2\text{W}_2\text{Ti}_4\text{Nb}_4\text{O}_{30}$) have shown extremely intriguing electrical properties, which can be further explored for possible device applications. Utilizing such materials for nonlinear optical materials for second harmonic generation is one of the key goals.^{12–22}

In the present study, we substituted transition metal Fe and Mn in $\text{Ba}_{0.95}\text{Sr}_{0.05}\text{Ca}_5\text{Ti}_{2-x}\text{M}_x\text{Nb}_8\text{O}_{30}$ synthesized by solid-state reaction. The aim was to determine the (i) variation in structural modifications from Mn or Fe substitution, (ii) the optical and magnetic properties, and (iii) the electrical modification by impedance spectroscopy as a function of Mn or Fe content in order to understand the relationship between the electrical, optical, magnetic, and structural parameters of the $\text{Ba}_{0.95}\text{Sr}_{0.05}\text{Ca}_5\text{Ti}_{2-x}\text{M}_x\text{Nb}_8\text{O}_{30}$ ceramics.

Experimental

Materials and Methods

The solid-state reaction method holds great value in various fields, particularly in materials science based on atomic-level close mixing. With this process, the dopants are uniformly distributed throughout the ceramic matrix, which is essential for obtaining the appropriate structural and electrical properties, making it possible to precisely control the stoichiometry of the final product. The composition of the ceramic material can be optimized by varying the reactant ratios, which is crucial for maximizing its ferroelectric characteristics. In comparison with other synthesis routes such as sol–gel, hydrothermal, or chemical vapor deposition, solid-state reaction is often preferred for its simplicity, cost-effectiveness, and suitability for producing bulk quantities of doped ferroelectric ceramics with controlled composition. In this work, stoichiometric ratios of barium carbonate (BaCO_3), strontium carbonate (SrCO_3), calcium carbonate (CaCO_3), titanium oxide (TiO_2), and niobium oxide (Nb_2O_5) were used to synthesize pure and Fe-doped $\text{Ba}_{0.95}\text{Sr}_{0.05}\text{Ca}_5\text{Ti}_2\text{Nb}_8\text{O}_{30}$ (BSCTN). Pure BSCTN samples were prepared using the solid-state reaction technique. The materials were ground for 5–6 h before undergoing calcination in a muffle furnace at 1150 °C for 2 h. Following calcination, the samples were ground again with a drop of polyvinyl alcohol (PVA) as a binder in calcined powder before being pelletized in a hydraulic press at 300 MPa pressure. To improve sample densification, the pellets were reintroduced into the muffle furnace for sintering at 1250 °C for 2 h.



Characterization Techniques

X-ray diffraction (XRD) patterns of the powder sample were investigated with a Philips x-ray diffractometer using Cu K α radiation ($\lambda = 1.540 \text{ \AA}$) at a scanning rate of 0.02°/s from 20° to 80° with 0.02 step size. Scanning electron microscopy (SEM) was performed using a Carl Zeiss Sigma 500 instrument. The pellet was shaped like a disc capacitor, with the specimen serving as the dielectric medium for dielectric properties. In preparation for use as an electrode, both flat surfaces of the sintered pellet (1 mm thickness and 10 mm diameter) were polished and silver paste was applied. For dielectric measurements, an LCR meter (Hioki 3532 50 LCR HiTester) was utilized. The infrared (IR) spectra of the sample were acquired with Fourier transform infrared (FTIR) spectroscopy in the range of 400–4000 cm^{-1} using a PerkinElmer FTIR spectrometer and KBr with Spectrum 10 software. The photoluminescence emission spectra (PLS) of powder samples were measured at room temperature using a spectrofluorophotometer with a xenon arc lamp as a light source and 400 nm excitation wavelength. The magnetic properties of the materials were assessed at room temperature using vibrating-sample magnetometry (VSM; Lake Shore 7410-S magnetometer).

Results and Discussion

Structural Analysis

The results of Rietveld refinement of the XRD data for the $\text{Ba}_{0.95}\text{Sr}_{0.05}\text{Ca}_5\text{Ti}_{2-x}\text{M}_x\text{Nb}_8\text{O}_{30}$ (where M is Fe and Mn and x is 0 and 0.05) powder are shown in Fig. 1a. All the ceramics were single-phase with a tungsten-bronze structure (space group Pbcn), according to the refinement results.

As can be seen in Fig. 1b–d, the smallest difference between the experimental data (shown by black line) and estimated data (shown by red line) from the x-ray patterns was found for $\text{Ba}_{0.95}\text{Sr}_{0.05}\text{Ca}_5\text{Ti}_{2-x}\text{M}_x\text{Nb}_8\text{O}_{30}$. The best way to verify the effectiveness and quality of the refinement is to compare the calculated and measured data differences. According to previous research, the reliability index parameters (R -values), i.e., R -profile (R_p), R -weighted profile (R_{wp}), expected residual factor (R_{exp}), and goodness of fit (GOF), have generally been used to verify the quality and validity of the various data from structural refinement. The following equations describe the chosen R -values:

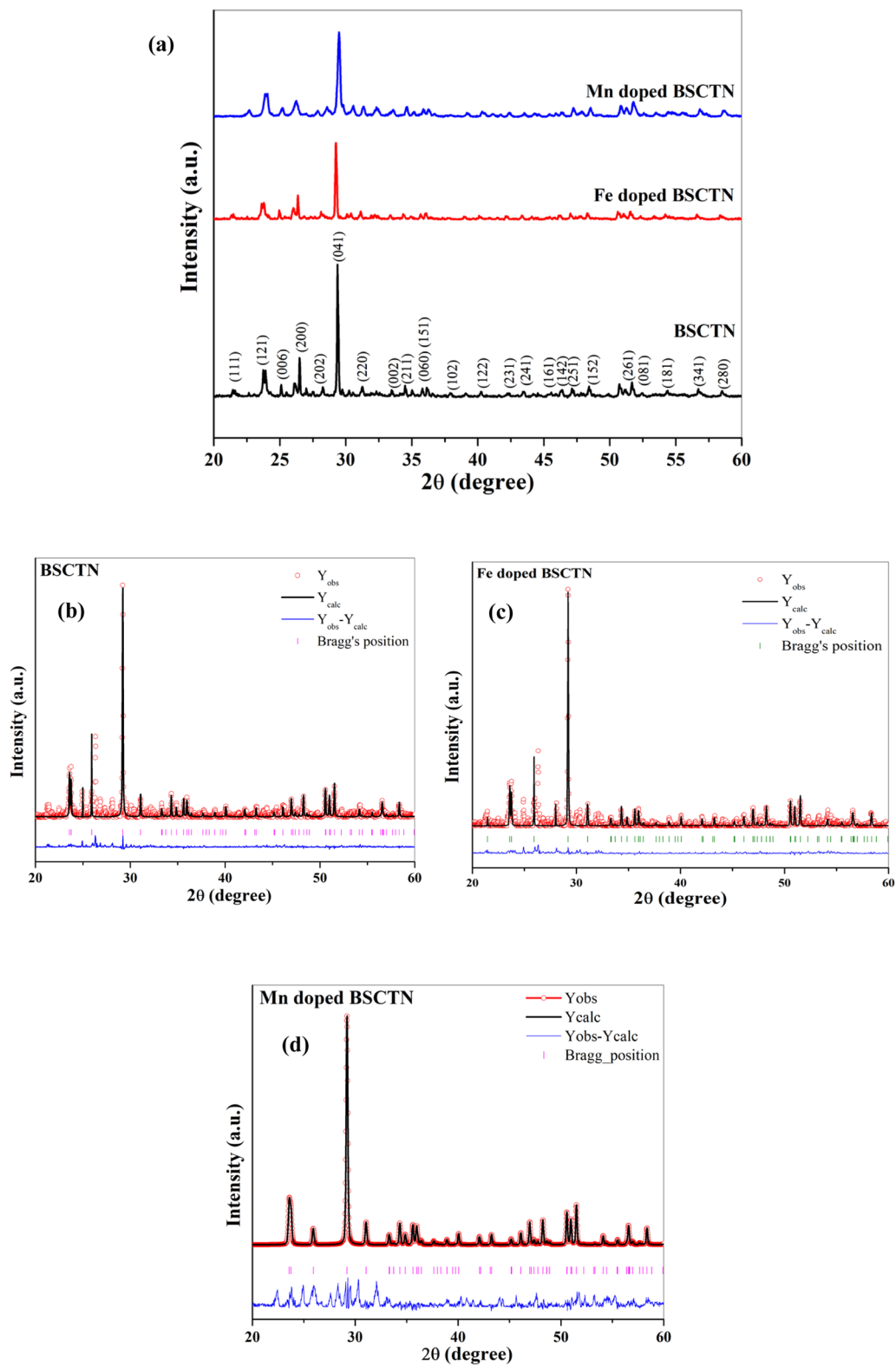


Fig. 1 (a) XRD pattern and results of Rietveld refinement of (b) BSCTN, (c) Fe-doped BSCTN, and (d) Mn-doped BSCTN powders.

Profile factor:

$$R_p = \left[\frac{\sum_i |Y_i^{\text{obs}} - Y_i^{\text{calc}}|}{\sum_i Y_i^{\text{obs}}} \right] \quad (1)$$

Weighted factor:

$$R_{wp} = \left[\frac{\sum_i w_i |Y_i^{\text{obs}} - Y_i^{\text{calc}}|^2}{\sum_i w_i Y_i^{\text{obs}^2}} \right]^{1/2} \quad (2)$$

Chi-squared factor (or GOF):

$$\chi^2 = \left[\frac{R_{wp}}{R_E} \right]^2 \quad (3)$$

where w_i is weight, and Y_i^{obs} and Y_i^{calc} are the measured and estimated intensities of the reflections at 2θ angles, respectively. R_p is the number of refined parameters, while N denotes the number of measurement points. The GOF, which is dependent on R_{wp} and R_{exp} and should be less than 2 for the best fit of the Rietveld analysis, is clear from the aforementioned equations. Good agreement was achieved between the calculated and observed model. Table 1 lists the experimental settings and structural information for the $\text{Ba}_{0.95}\text{Sr}_{0.05}\text{Ca}_5\text{Ti}_{2-x}\text{M}_x\text{Nb}_8\text{O}_{30}$, $\text{Ba}_{0.95}\text{Sr}_{0.05}\text{Ca}_5\text{Ti}_{1.95}\text{Fe}_{0.05}\text{Nb}_8\text{O}_{30}$, and $\text{Ba}_{0.95}\text{Sr}_{0.05}\text{Ca}_5\text{Ti}_{1.95}\text{Mn}_{0.05}\text{Nb}_8\text{O}_{30}$ powder. To demonstrate the effect of Fe and Mn substitution in the XRD pattern, a magnified XRD graph shows a peak around 29° , indicating the shifting of the peak towards the lower angle. The decrease in peak intensity with doping indicates that when Fe or Mn is introduced into B_1 or B_2 sites, the crystal structure is somewhat distorted. The crystallite size and strain calculated by the Scherrer formula and Williamson–Hall

(W-H) plot are shown in Fig. 2a and b, respectively, based on composition.

The tolerance factor was computed for each composition using Eqs. 4 and 5:

$$t_{A1} = \frac{R_{A1} + R_O}{\sqrt{2}(R_B + R_O)} \quad (4)$$

$$t_{A2} = \frac{R_{A2} + R_O}{\sqrt{23} - 12\sqrt{3}(R_B + R_O)} \quad (5)$$

where R_A , R_B , and R_O denote the A-site, B-site, and oxygen ionic radii, respectively. Figure 2c depicts the estimated tolerance factor, which suggests that the value of t is smaller than 1 for all compositions, indicating a stable orthorhombic structure.^{11,23,24} The electronegativity was also estimated by varying the given formula based on composition.^{28,29} The improved formula (for BSCTN) is given in Eq. 6:

$$e = \frac{0.95\chi_{\text{Ba-O}} + 0.05\chi_{\text{Sr-O}} + 5\chi_{\text{Ca-O}} + 2\chi_{\text{Ti-O}} + 8\chi_{\text{Nb-O}}}{32} \quad (6)$$

where χ represents the corresponding electronegativity values for particular bonds. The values for all of the compositions using the formula are plotted in Fig. 2c. As electronegativity increases, so does the bond dissociation energy. The basic ferroelectric phenomena are caused by electrical interaction between the constituent atoms. In reality, the electronegativity of a single element varies between compounds. It may wander to either side of the required value depending on the coordination number, bond change, formal charges, and the character of the neighboring atoms. As a result, it was formerly thought that the chemical bonds in ferroelectric structures functioned as a sort of bridge between the ionic and covalent states, resulting in changes in bond lengths, bond angles, and lattice deformation. In our investigation, the value of electronegativity increased, indicating that doping improved the ferroelectric properties.^{1,2,22,23}

SEM images of the surface of $\text{Ba}_{0.95}\text{Sr}_{0.05}\text{Ca}_5\text{Ti}_{2-x}\text{M}_x\text{Nb}_8\text{O}_{30}$ (where M is Fe and Mn and x is 0 and 0.05) pellets sintered at 1250°C for 6 h are shown in Fig. 3a, from which we can infer that the material has a thick microstructure and that the uneven grain sizes are uniformly distributed throughout the sample's surface. In addition, 96% of the theoretical density can be found in the relative density. The average grain size of pure BSCTN ceramic is $1.25\ \mu\text{m}$, for Fe-doped BSCTN is $2\ \mu\text{m}$, and for Mn-doped BSCTN is $2.5\ \mu\text{m}$, according to the histogram shown in Fig. 3b.

Figure 4 presents the spectra for the FTIR spectroscopy results for BSCTN, Fe-doped BSCTN, and Mn-doped BSCTN. The as-prepared materials have an orthorhombic structure with space group Pbcn, according to the x-ray diffraction analysis. FTIR spectra were also recorded

Table 1 Parameters of BSCTN, Fe-doped BSCTN, and Mn-doped BSCTN calculated from XRD

Composition	BSCTN	Fe-doped BSCTN	Mn-doped BSCTN
Crystal system	Orthorhombic	Orthorhombic	Orthorhombic
Space group	Pbcn	Pbcn	Pbcn
Lattice parameter			
a (Å)	14.966	14.969	14.966
b (Å)	5.749	5.752	5.773
c (Å)	5.220	5.220	5.320
R- factors			
R_p (%)	5.7	8.4	7.4
R_w (%)	7.8	11.1	12.2
GOF (χ^2)	1.87	1.83	1.64

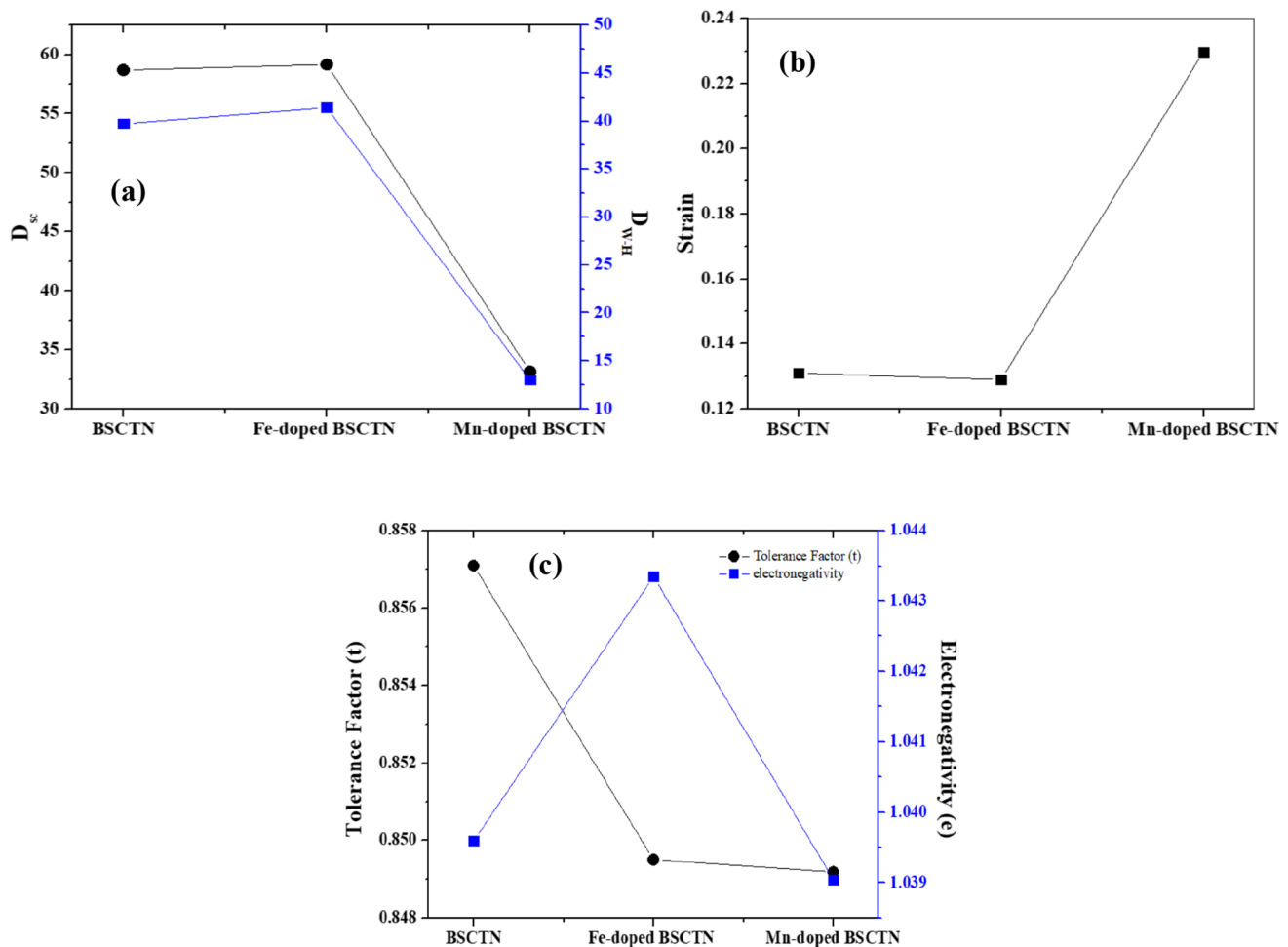


Fig. 2 (a) Crystallite size (a) and strain (b) calculated by the Scherrer formula (D_{SC}) and W-H plot (D_{W-H}); (c) tolerance factor and electronegativity of BSCFN, Fe-doped BSCFN, and Mn-doped BSCFN.

within the range of 4000 to 400 cm^{-1} in order to probe the structural intricacies of the prepared materials, and are displayed in Fig. 4. Prominent peaks are visible in the fingerprint region from 900 cm^{-1} to 400 cm^{-1} , shown in the inset graph of Fig. 4. Absorption bands corresponding to Nb–O stretching vibrations are located at 869 cm^{-1} (ν_1 mode of vibration) and 744 cm^{-1} (ν_2 mode of vibration). The ν_3 mode of vibration and the stretching vibrations of the Nb–O and Ti–O bonds are responsible for the broad band at about 590 cm^{-1} . Similarly, the band at 488 cm^{-1} may be caused by O–Nb/Ti–O bond bending vibrations (ν_4 mode of vibration).

Thus, a somewhat distorted (NbO_6 octahedra) crystal structure is indicated by variables such as Nb–O stretching, O–Nb–O bending, and Ca–O stretching vibrations affecting chain bonds, and broadening of the peaks.¹

Magnetic Properties

Figure 5a displays VSM plots that provide information on the material's magnetic characteristics via doping of Fe and Mn transition metals at room temperature. Pure BSCFN shows a diamagnetic nature. However, the substitution of transition metals has caused a shift in the magnetic properties. Both Fe and Mn show a tendency to rotate the plot, but Fe has a greater tendency to cause the plot to shift from diamagnetic to ferromagnetic behavior. The photoluminescence (PL) activity of the samples was examined by measuring the PL emission spectra of the samples. Figure 5b displays the acquired PL spectra at an excitation wavelength of 400 nm . The sample exhibits good luminescence properties in the visible spectrum. Payling and Larkins¹⁹ used the data to identify the transmission accountable for each emission. The emission peak at 421 nm is due

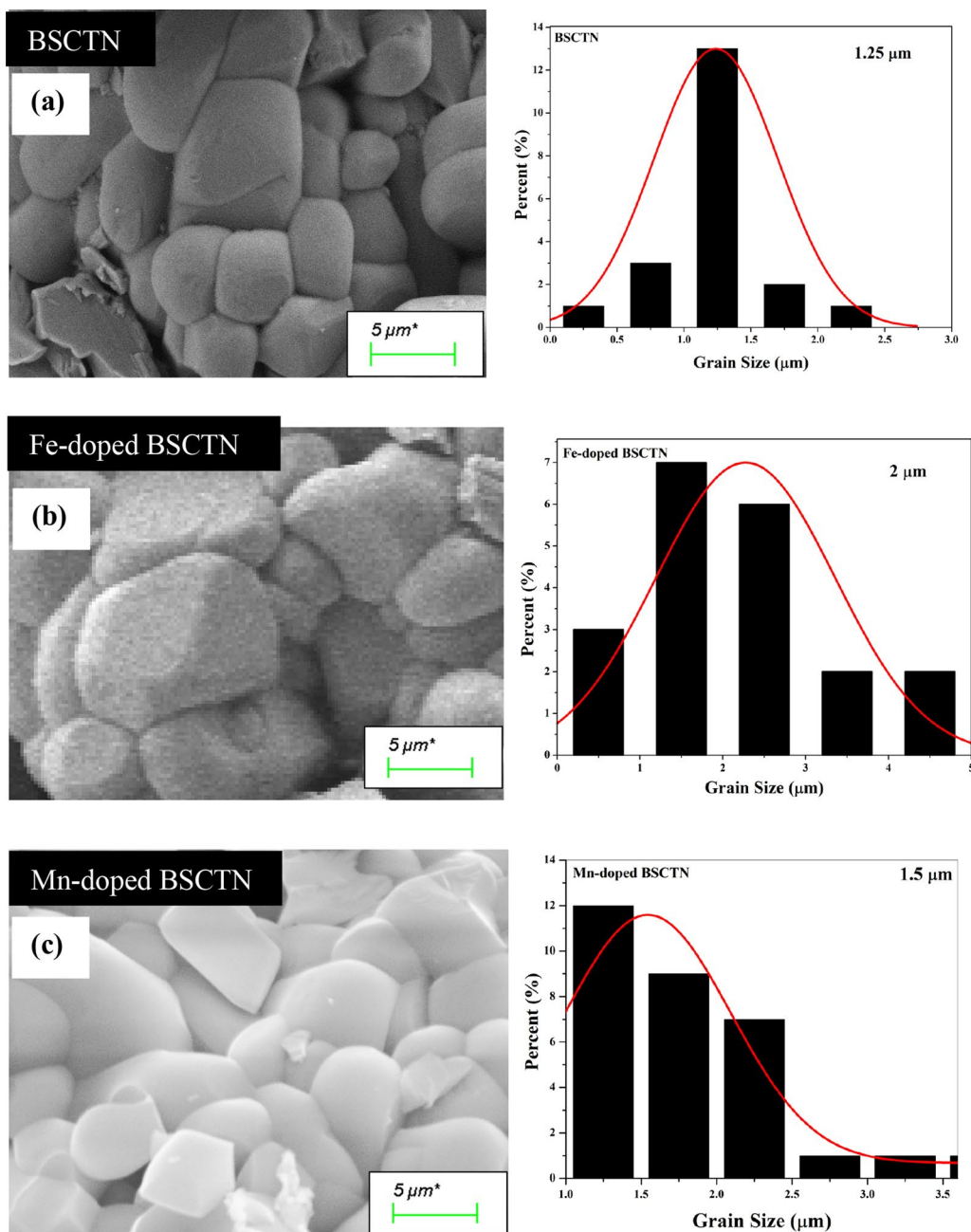


Fig. 3 SEM images along with probability distribution graph of (a) BSCTN, (b) Fe-doped BSCTN, and (c) Mn-doped BSCTN.

to the ${}^4S_{01.5} \rightarrow {}^4D_{1.5}$ transition of O, while the emission peaks at 512 and 621 nm are assigned to the ${}^3D_1 \rightarrow {}^1P_01$ transition of Nb and the $f-f$ transition of Nb/Ti, respectively. Apart from their different electronic transitions, the Jahn–Teller (JT) effect is also responsible for some changes in the PL spectra of the doped materials. Additional peaks are observed in Mn-doped BSCTN which correspond to the addition of Mn to Pure BSCTN. The energy bandgap was computed for these peaks in the range of 2 to 3 eV. The samples have strong emission

lines at a particular wavelength, making the material suitable for optoelectronic applications.

Impedance Analysis

Complex impedance spectroscopy provides information about the impact of grains, grain boundaries, and electrodes on the capacitive, resistive, and inductive properties of a material. The real and imaginary parts of impedance are depicted in Fig. 6a. The real part of the impedance

decreases and converges to zero. Because the three compounds have multicomponent polarization, including electronic, ionic, orientational, and interfacial polarization, the real part of the impedance Z' has a high value at low frequencies. However, when the frequency increases, the dipolar orientation and interfacial polarization contributions diminish, resulting in a constant value of the real part of the impedance Z' . The reduction in Z' with the increase in frequency and temperature suggests an increase in AC conductivity. The reduction in Z' with rising temperature at low frequencies suggests negative temperature coefficient of resistance (NTCR) behavior. Figure 6b shows the imaginary component of impedance, where peaks are clearly apparent in the pure and doped

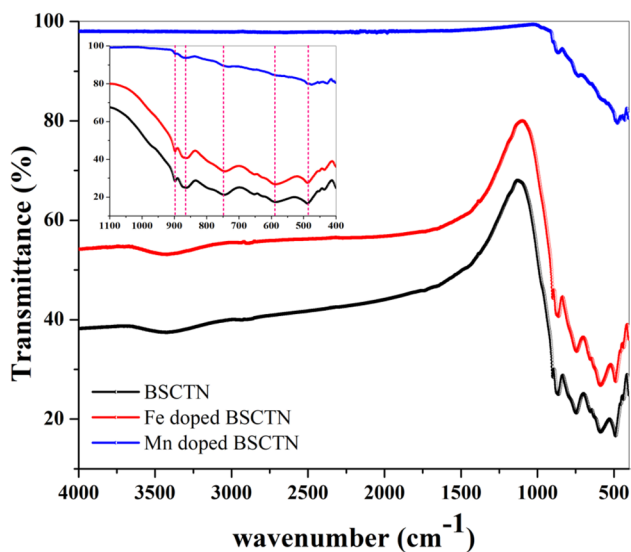


Fig. 4 FTIR spectrum (enlarged view of fingerprint region shown in inset graph) of BSCTN, Fe-doped BSCTN, and Mn-doped BSCTN

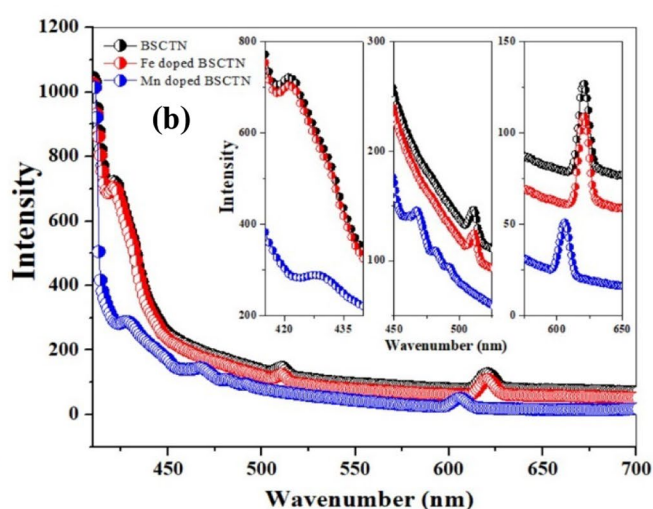
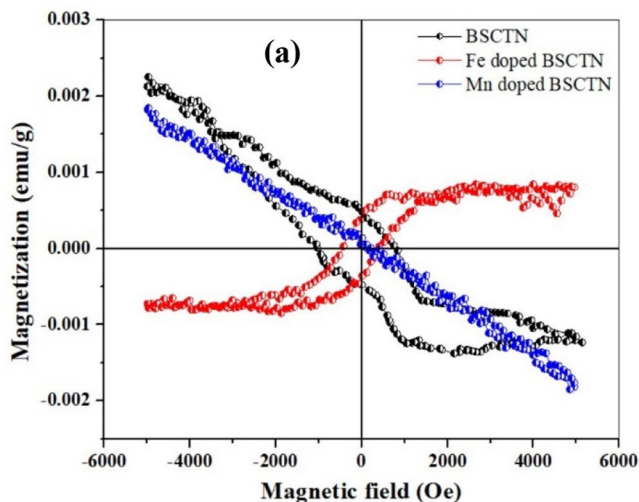


Fig. 5 (a) VSM plots and (b) PL spectra for BSCTN, Fe-doped BSCTN, and Mn-doped BSCTN.

material spectra. The peak amplitude of Z'' is known as Z''_{\max} , and the associated frequency (f_{\max}) is known as the relaxation frequency. At low temperatures, the relaxation frequency (f_{\max}) is modest, which indicates that moving load carriers (OVs) require a long time to move from one location to another. The value of Z''_{\max} drops as the temperature increases, but f_{\max} shifts to higher frequencies as the temperature increases. This shift in the maximum frequency to higher frequencies suggests that the relaxation time decreases as temperature increases. The Nyquist plot is a plot of the imaginary part (Z'') of impedance as a function of the real part (Z'), shown in Fig. 6c. Semicircular arcs are observed in these variations. The simulation of the experimental data using the appropriate equivalent electrical circuit using ZView software revealed that the results correspond well to the series connection of two cells which are associated with grain and grain boundary effects, respectively. Figure 6d depicts the appropriate equivalent circuit for the BSCTN. The equivalent circuit that is used to fit the data is made up of two parts, Rg or R1 and Cg or C1, which represent the resistance and capacitance of the grain in the first parallel circuit linked to the grain contribution, and Rgb or R2 and Cgb or C2, which represent the resistance and capacitance of the grain boundary in the second parallel circuit. The semicircular arcs were suited for the (R1C1)(R2C2) circuit. ^{11,19,22–29}

Dielectric Properties

Dielectric data ($\epsilon^* = \epsilon' - j\epsilon''$) were calculated from complex impedance data ($Z^* = Z' + jZ''$) using the following expressions³⁰

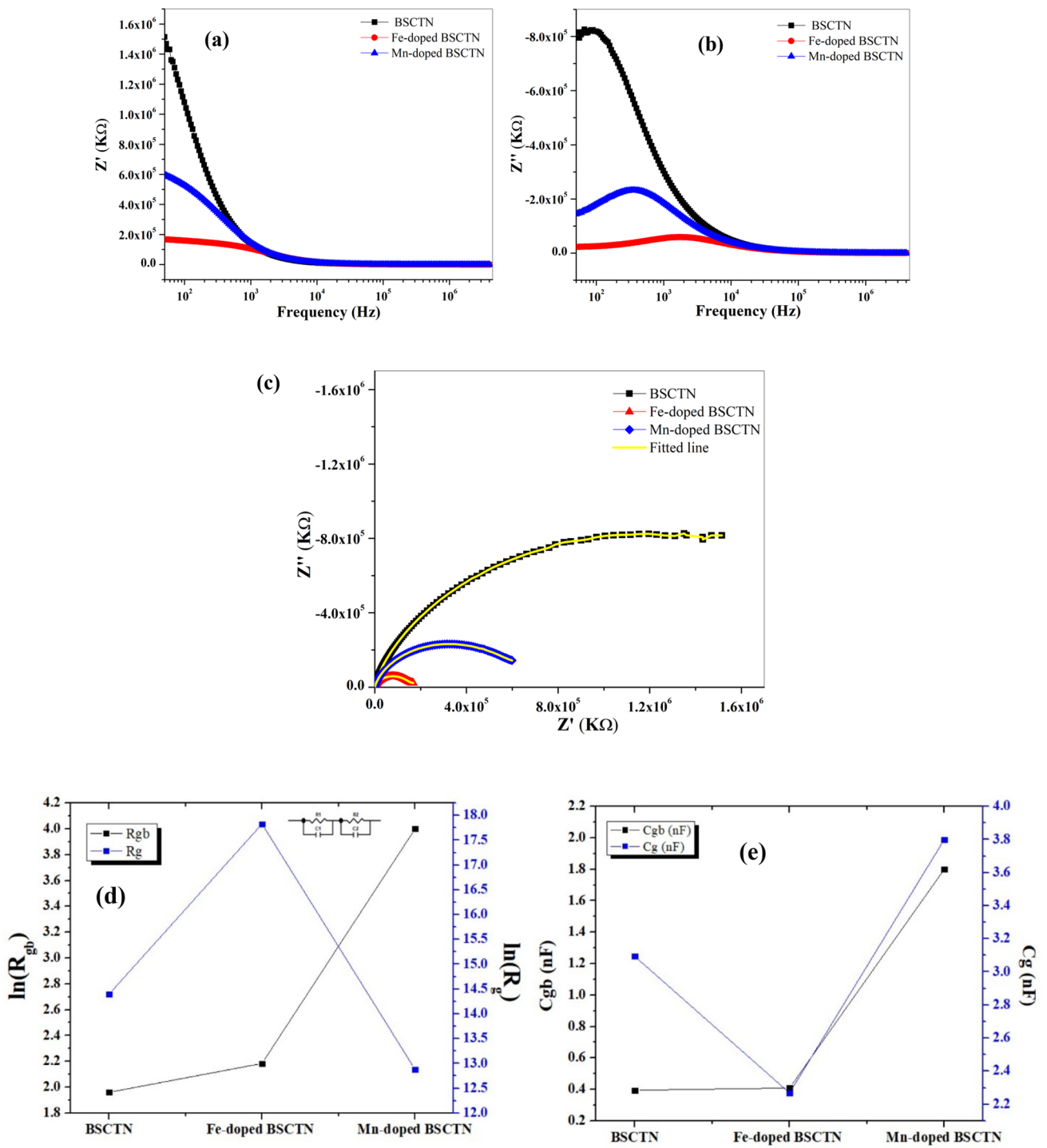


Fig. 6 (a) Real part of impedance versus frequency, (b) imaginary part of impedance versus frequency, (c) Nyquist plots, (d) $\ln R_g$ and $\ln R_{gb}$ and (e) C_g and C_{gb} plots of BSCTN, Fe-doped BSCTN, and Mn-doped BSCTN.

$$\epsilon' = \frac{t}{\omega * A * \epsilon_o} \cdot \frac{-Z''}{Z'^2 + Z''^2} \tag{7}$$

$$\epsilon'' = \frac{t}{\omega * A * \epsilon_o} \cdot \frac{Z'}{Z'^2 + Z''^2} \tag{8}$$

The tangent loss for the material can be calculated by taking the ratio of the imaginary part to the real part of the dielectric permittivity and can be expressed as

$$\tan\delta = \frac{\epsilon''}{\epsilon'} \quad (9)$$

Figure 7a shows the variation in dielectric permittivity with frequency at room temperature. From 10 Hz to 100 Hz, it is evident that the dielectric constant decreases rapidly and becomes almost constant at frequencies over 100 Hz. It is widely known that dielectric materials demonstrate a steady drop in dielectric constant with increasing

frequency. The dipole, atomic, ionic, electronic, and other forms of polarization that these materials have are responsible for their high permittivity in the low-frequency area. The relative permittivity drops and reaches a plateau at high frequencies; this behavior suggests the presence of charged species (oxygen vacancies, grain boundary effects, etc.) that are unable to track changes in the applied alternating electric field at high frequencies. Figure 7b shows the decreasing trend of tangent loss for all the samples, which can be attributed to space charge polarization. Figure 8a depicts the variation in dielectric constant with temperature at a constant frequency of 1 MHz between 35 °C and 300 °C. Peaks can be clearly observed for all

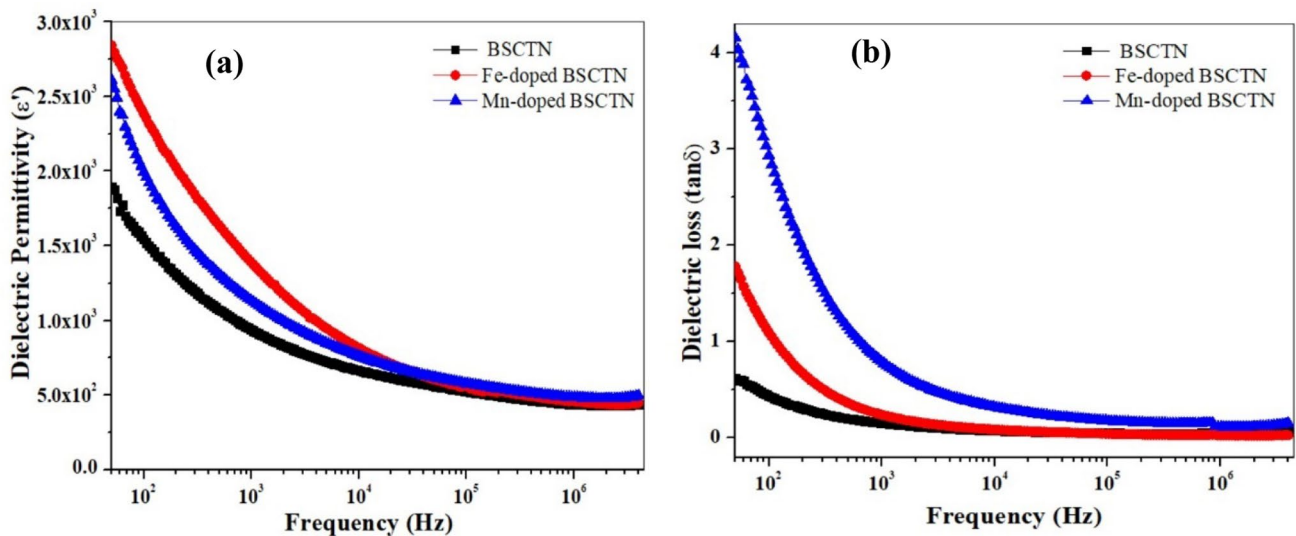


Fig. 7 (a) Variation in dielectric permittivity and (b) dielectric loss with frequency at room temperature for BSCTN, Fe-doped BSCTN, and Mn-doped BSCTN.

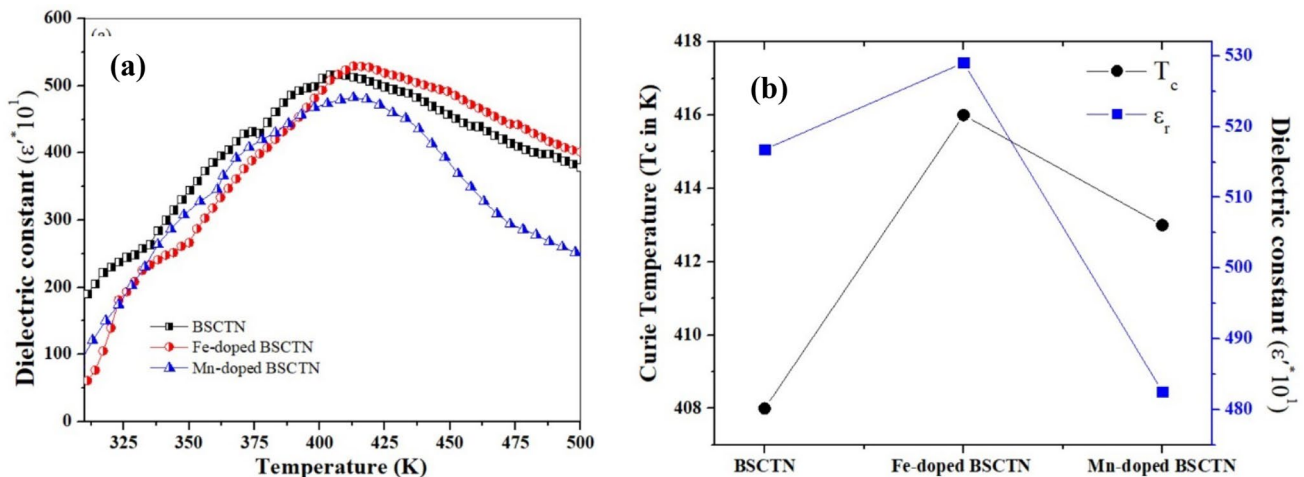


Fig. 8 (a) Variation in dielectric constant with temperature at 1 MHz and (b) variation in Curie temperature (T_c) and dielectric constant with composition (ϵ) for BSCTN, Fe-doped BSCTN, and Mn-doped BSCTN

three ceramics. The peaks correspond to the orthorhombic (Pbcn) ferroelectric phase transitioning to the paraelectric phase. At all frequencies, all three materials have the same Curie temperature (T_C), indicating that they do not exhibit relaxor behavior. The dielectric peak is discovered to have expanded, signifying the occurrence of a diffuse phase transition. Figure 8b shows the evolution of the Curie temperature and dielectric constant of the doped and undoped samples. It is observed that the Fe-doped compound has a higher Curie temperature than pure and Mn-doped compound, indicating that Fe-doped compound exhibit more significant ferroelectric characteristics.^{23,29}

Modulus Study

A useful method for examining electrical transport events in ceramics and identifying the microscopic mechanisms responsible for dielectric relaxation is the analysis of the complex dielectric modulus. The complex modulus equation can be written in the form

$$M^* = \frac{1}{\epsilon^*} = M' + jM'' \quad (10)$$

where M' and M'' represent the real and imaginary parts of the modulus, which can be represented as follows:

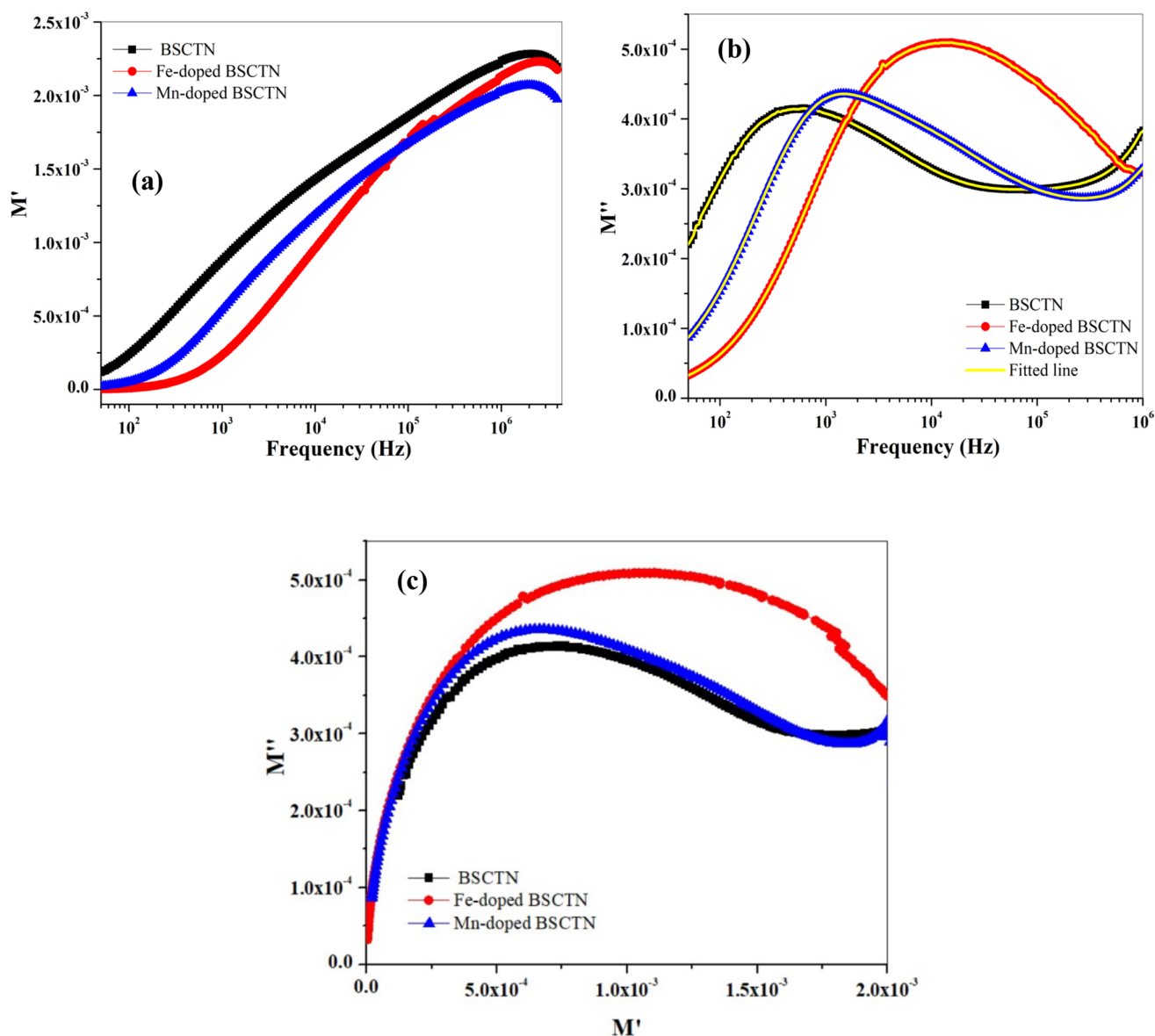


Fig. 9 Changes in the (a) real and (b) imaginary parts of the modulus with frequency and (c) M' versus M'' for BSCTN, Fe-doped BSCTN, and Mn-doped BSCTN.

$$M' = \frac{\epsilon'}{(\epsilon')^2 + (\epsilon'')^2} \quad (11)$$

$$M'' = \frac{\epsilon''}{(\epsilon')^2 + (\epsilon'')^2} \quad (12)$$

where ϵ' and ϵ'' are the real and imaginary parts of the dielectric permittivity, respectively.³¹ Figure 9 displays the real and imaginary parts of the modulus with respect to frequency variation for all three compounds. When the real part of the modulus is considered (Fig. 9a), the values are closer to zero in the lower-frequency ranges and reach saturation in the higher-frequency ranges after increasing. Figure 9b shows the variation in the imaginary component of the modulus M'' as a function of frequency. Three distinct regions are observed. The first zone is at lower frequencies, where charge carriers can hop from one location to another. They can only move within the well and can only move a limited distance in the second region. The final zone is near the top of the M'' peak, where the change from long-distance to short-distance mobility takes place. The presence of a stretching component is shown by the asymmetric broadening of the peaks, which validates the type of relaxation process. This behavior was confirmed by fitting from Bergman's modified Kohlrausch–Williams–Watts (KWW) function as given in Eq. 13:

$$M'' = \frac{M''_{\max}}{(1 - \beta) + \frac{\beta}{1 + \beta} \left[\beta \left(\frac{f_{\max}}{f} \right) + \left(\frac{f}{f_{\max}} \right)^\beta \right]} \quad (13)$$

where M''_{\max} is the maximum value of M'' , f_{\max} is the maximum frequency, and β is the stretched exponent. When $\beta = 1$, a perfect Debye type relaxation occurs, and when $\beta = 0$ to < 1 , a non-Debye type relaxation occurs. Table II displays the values derived for β , confirming the non-Debye relaxation for the pure and doped samples. Figure 9c depicts the variation in M' and M'' with $x = 0$ frequency. The variation depicts the frequency crossover point. It exhibits Debye-like behavior before crossing the point, and when the frequency increases, the variation verifies Arrhenius behavior and the non-Debye process.^{29,31–33}

We have performed experiments to enhance the electrical and magnetic properties of tungsten bronze ferroelectric ceramics by substitution of transition metals. However, other researchers have employed simulation studies and machine learning for the development of sustainable materials,^{34–37} which can reduce costly experimentation with different kinds of materials. Simulation studies have also been shown to control the magnetic behavior of materials for space propulsion applications.^{38,39}

Table II Parameters calculated from fitting the imaginary part of the modulus data

Composition (x)	FWHM (for M'')	β
BSCTN	9.354	0.872
Fe-doped BSCTN	7.527	0.760
Mn-doped BSCTN	4.296	0.442

Conclusion

The solid-state reaction method was used to successfully synthesize $\text{Ba}_{0.95}\text{Sr}_{0.05}\text{Ca}_5\text{Ti}_{2-x}\text{M}_x\text{Nb}_8\text{O}_{30}$ ceramics, where M is Fe and Mn and x is 0 and 0.05. Rietveld analysis of the XRD data revealed a pure orthorhombic tungsten bronze structure with the Pbcn space group for all samples. SEM analysis revealed a homogeneous microstructure with unequal grain sizes, strong densification, and low porosity. The average grain size was in the range of 1–2 μm . The Fe-doped BSCTN exhibited grain size of approximately 2 μm , which was higher than that of the undoped and Mn-doped BSCTN. Impedance spectroscopy results showed that the theoretical simulation successfully explained the experimental data of the Nyquist plot, and it was revealed that grains and grain boundaries both contributed to the conduction process. The replacement of Ti^{4+} for Mn^{3+} and Fe^{3+} increased the resistance value of the $\text{Ba}_{0.95}\text{Sr}_{0.05}\text{Ca}_5\text{Ti}_{2-x}\text{M}_x\text{Nb}_8\text{O}_{30}$ ceramics for grains and grain boundaries. Investigation of the variation in the dielectric permittivity of the pure and doped BSCTN with frequency at room temperature revealed that the maximum dielectric permittivity and higher Curie temperature (T_C) were shown by the Fe-doped sample ($T_C = 413$ K and $\epsilon_r = 2843.41$), indicating better ferroelectric properties than those of the undoped ($T_C = 403$ K and $\epsilon_r = 1895.36$) and Mn-doped samples ($T_C = 410$ K and $\epsilon_r = 2609.66$). The modulus plot, i.e., M'' versus M' , demonstrated the contribution of grains and grain boundaries, and the asymmetric nature of the imaginary part of the modulus indicated that relaxation processes observed in the ceramics were non-Debye in nature by KWW fitting, and the corresponding values of the β parameter ranged from 0 to 1, confirming the non-Debye relaxation for pure and doped samples.

Conflict of Interest The authors declare that they have no conflict of interest.

References

1. K.C. Mathai, S. Vidya, A. John, S. Solomon, and J.K. Thomas, Structural, optical, and compactness characteristics of nanocrystalline CaNb_2O_6 synthesized through an autoigniting combustion

- method. *Adv. Condens. Matter Phys.* 2014, 1–6 (2014). <https://doi.org/10.1155/2014/735878>.
- P. Ganguly and A.K. Jha, Structural and electrical properties of $\text{Ba}_{5-x}\text{Ca}_x\text{SmTi}_3\text{Nb}_7\text{O}_{30}$ ($x=0-5$) ferroelectric ceramics. *J. Alloy. Compd.* 495, 7–12 (2010). <https://doi.org/10.1016/j.jallcom.2010.01.118>.
 - X. Zhu, M. Fu, M.C. Stennett, P.M. Vilarinho, I. Levin, C.A. Randall, J. Gardner, F.D. Morrison, and I.M. Reaney, A crystal-chemical framework for relaxor versus normal ferroelectric behavior in tetragonal tungsten bronzes. *Chem. Mater.* 27, 3250–3261 (2015). <https://doi.org/10.1021/acs.chemmater.5b00072>.
 - A. Rotaru and F.D. Morrison, Vogel-Fulcher analysis of relaxor dielectrics with the tetragonal tungsten bronze structure: $\text{Ba}_6\text{MNb}_9\text{O}_{30}$ ($M = \text{Ga}, \text{Sc}, \text{In}$). *J. Therm. Anal. Calorim.* 120, 1249–1259 (2015). <https://doi.org/10.1007/s10973-014-4355-5>.
 - X.L. Zhu, K. Li, and X.M. Chen, Ferroelectric transition and low-temperature dielectric relaxations in filled tungsten bronzes. *J. Am. Ceram. Soc.* 97, 329–338 (2014). <https://doi.org/10.1111/jace.12790>.
 - X.L. Zhu, S.Y. Wu, and X.M. Chen, Dielectric anomalies in $(\text{Ba}_x\text{Sr}_{1-x})_4\text{Nd}_2\text{Ti}_4\text{Nb}_6\text{O}_{30}$ ceramics with various radius differences between A1- and A2-site ions. *Appl. Phys. Lett.* (2007). <https://doi.org/10.1063/1.2800789>.
 - M.C. Stennett, I.M. Reaney, G.C. Miles, D.I. Woodward, A.R. West, C.A. Kirk, and I. Levin, Dielectric and structural studies of $\text{Ba}_2\text{MTi}_2\text{Nb}_3\text{O}_{15}$ (BMTNO₁₅, $M=\text{Bi}^{3+}, \text{La}^{3+}, \text{Nd}^{3+}, \text{Sm}^{3+}, \text{Gd}^{3+}$) tetragonal tungsten bronze-structured ceramics. *J. Appl. Phys.* (2007). <https://doi.org/10.1063/1.2205720>.
 - P. Ganguly and A.K. Jha, Investigations of structural, dielectric and electrical behaviour of calcium substituted $\text{Ba}_5\text{NdTi}_3\text{Nb}_7\text{O}_{30}$ ferroelectric ceramics. *Integr. Ferroelectr. Ferroelectr.* 115, 149–156 (2010). <https://doi.org/10.1080/10584587.2010.488566>.
 - X.L. Zhu, X.Q. Liu, and X.M. Chen, Crystal structure and dielectric properties of $\text{Sr}_5\text{RTi}_3\text{Nb}_7\text{O}_{30}$ ($R=\text{La}, \text{Nd}, \text{Sm}, \text{and Eu}$) tungsten bronze ceramics. *J. Am. Ceram. Soc.* 94, 1829–1836 (2011). <https://doi.org/10.1111/j.1551-2916.2010.04327.x>.
 - X. Li Zhu, Y. Bai, X.Q. Liu, and X. Ming Chen, Ferroelectric phase transition and low-temperature dielectric relaxations in $\text{Sr}_4(\text{La}_{1-x}\text{Sm}_x)_2\text{Ti}_4\text{Nb}_6\text{O}_{30}$ ceramics. *J. Appl. Phys.* (2011). <https://doi.org/10.1063/1.3664857>.
 - K. Li, X.L. Zhu, X.Q. Liu, and X.M. Chen, Effects of Ca-substitution on structural, dielectric, and ferroelectric properties of $\text{Ba}_5\text{SmTi}_3\text{Nb}_7\text{O}_{30}$ tungsten bronze ceramics. *Appl. Phys. Lett.* 101, 042906 (2012). <https://doi.org/10.1063/1.4739841>.
 - R.N.P. Choudhary, S.R. Shannigrahi, and A.K. Singh, Ferroelectric phase transition in $\text{Ba}_5\text{RTi}_3\text{Nb}_7\text{O}_{30}$ [$R=\text{Nd}, \text{Eu}, \text{Gd}$] ceramics. *Bull. Mater. Sci.* 22, 975–979 (1999). <https://doi.org/10.1007/bf02745689>.
 - P.P. Rao, S.K. Ghosh, and P. Koshy, Dielectric and ferroelectric properties of $\text{Ba}_3\text{M}_3\text{Ti}_5\text{Nb}_5\text{O}_{30}$ ($M = \text{Sm}$ or Y) ceramics. *J. Mater. Sci.: Mater. Electr.* 12, 729–732 (2001). <https://doi.org/10.1023/A:1012944927315>.
 - S.R. Shannigrahi, R.N.P. Choudhary, A. Kumar, and H.N. Acharya, Phase transition in $\text{Ba}_5\text{RTi}_3\text{Nb}_7\text{O}_{30}$ ($R = \text{Dy}, \text{Sm}$) ferroelectric ceramics. *J. Phys. Chem. Solids* 59, 737–742 (1998). [https://doi.org/10.1016/s0022-3697\(97\)00217-5](https://doi.org/10.1016/s0022-3697(97)00217-5).
 - X.H. Zheng and X.M. Chen, Dielectric ceramics with tungsten-bronze structure in the $\text{BaO}-\text{Nd}_2\text{O}_3-\text{TiO}_2-\text{Nb}_2\text{O}_5$ system. *J. Mater. Res.* 17, 1664–1670 (2002). <https://doi.org/10.1557/jmr.2002.0245>.
 - P.R. Das, R.N.P. Choudhary, and B.K. Samantray, Diffuse ferroelectric phase transition in $\text{Na}_2\text{PbSm}_2\text{W}_2\text{Ti}_4\text{Nb}_4\text{O}_{30}$ ceramics. *Mater. Chem. Phys.* 101, 228–233 (2007). <https://doi.org/10.1016/j.matchemphys.2006.04.005>.
 - B. Behera, P. Nayak, and R.N.P. Choudhary, Structural, dielectric and electrical properties of $\text{NaBa}_2\text{X}_5\text{O}_{15}$ ($X=\text{Nb}$ and Ta) ceramics. *Mater. Lett.* 59, 3489–3493 (2005). <https://doi.org/10.1016/j.matlet.2005.06.019>.
 - J. Yeon, P.S. Halasyamani, and I.V. Kityk, Nonlinear optical effects in nano-sized ferroelectrics $\text{Sr}_6\text{Ti}_2\text{Nb}(\text{Ta})_8\text{O}_{30}$. *Mater. Lett.* 62, 1082–1084 (2008). <https://doi.org/10.1016/j.matlet.2007.07.048>.
 - V. Massarotti, D. Capsoni, M. Bini, C.B. Azzoni, M.C. Mozziati, P. Galinetto, and G. Chioldelli, Structural and spectroscopic properties of pure and doped $\text{Ba}_6\text{Ti}_2\text{Nb}_8\text{O}_{30}$ tungsten bronze. *J. Phys. Chem. B* 110, 17798–17805 (2006). <https://doi.org/10.1021/jp063382p>.
 - X.H. Zheng and X.M. Chen, Crystal structure and dielectric properties of ferroelectric ceramics in the $\text{BaO}-\text{Sm}_2\text{O}_3-\text{TiO}_2-\text{Nb}_2\text{O}_5$ system. *Solid State Commun.* 125, 449–454 (2003). [https://doi.org/10.1016/s0038-1098\(02\)00709-3](https://doi.org/10.1016/s0038-1098(02)00709-3).
 - L. Fang, H. Zhang, J.B. Yan, and W.M. Yang, Synthesis and dielectric properties of a new niobate $\text{Ba}_9\text{NdTi}_3\text{Nb}_7\text{O}_{30}$. *Chin. J. Inorg. Chem.* 18(11), 1131–1134 (2002).
 - A. Bendahhou, P. Marchet, A. El-Houssaine, S. El Barkany, and M. Abou-Salama, Relationship between structural and dielectric properties of Zn-substituted $\text{Ba}_5\text{CaTi}_{2-x}\text{Zn}_x\text{Nb}_8\text{O}_{30}$ tetragonal tungsten bronze. *CrystEngComm* 23, 163–173 (2021). <https://doi.org/10.1039/d0ce01561j>.
 - A. Bendahhou, P. Marchet, S. El Barkany, and M. Abou-salama, Structural and impedance spectroscopic study of Zn-substituted $\text{Ba}_5\text{CaTi}_2\text{Nb}_8\text{O}_{30}$ tetragonal tungsten bronze ceramics. *J. Alloy. Compd.* 882, 160716 (2021). <https://doi.org/10.1016/j.jallcom.2021.160716>.
 - S. Jindal, A. Vasisht, S. Devi, N. Aggarwal, and K.K. Kushwah, Investigation of structural, ferroelectric and magnetic properties of iron doped tungsten bronze multiferroic ceramics. *Physica B B* 595, 412341 (2020). <https://doi.org/10.1016/j.physb.2020.412341>.
 - S. Jindal, A. Vashishth, S. Devi, and K. Kumar Kushwah, Prospective features of multiferroic tungsten bronze ceramics and its futuristic applications. *Mater. Today: Proc.* 51, 1252–1258 (2022). <https://doi.org/10.1016/j.matpr.2021.07.351>.
 - S. Jindal, N. Aggarwal, A. Vasisht, and A. Sharma, Investigation of tungsten bronze ferroelectric ceramic by conventional and mechanical activation processes. *Mater. Today: Proc.* 68, 886–890 (2022). <https://doi.org/10.1016/j.matpr.2022.06.424>.
 - S. Jindal, S. Devi, A. Vasisht, K.M. Batoo, and G. Kumar, Interdependence between electrical and magnetic properties of polycrystalline cobalt-substituted tungsten bronze multiferroic ceramics. *J. Adv. Dielectr. Dielectr.* 08, 1850002 (2018). <https://doi.org/10.1142/s2010135x18500029>.
 - P. Sahoo, A. Panigrahi, S. Patri, and R. Choudhary, Structural, dielectric, electrical and piezoelectric properties of $\text{Ba}_4\text{SrTi}_3\text{V}_7\text{O}_{30}$ ($R=\text{Sm}, \text{Dy}$) ceramics. *Open Phys.* (2008). <https://doi.org/10.2478/s11534-008-0112-3>.
 - A. Bendahhou, K. Chourti, R. El Bouayadi, S. El Barkany, and M. Abou-Salama, Structural, dielectric and impedance spectroscopy analysis of $\text{Ba}_5\text{CaTi}_{1.94}\text{Zn}_{0.06}\text{Nb}_8\text{O}_{30}$ ferroelectric ceramic. *RSC Adv.* 10, 28007–28018 (2020). <https://doi.org/10.1039/d0ra05163b>.
 - J.H. Joshi, D.K. Kanchan, M.J. Joshi, H.O. Jethva, and K.D. Parikh, Dielectric relaxation, complex impedance and modulus spectroscopic studies of mix phase rod like cobalt sulfide nanoparticles. *Mater. Res. Bull.* 93, 63–73 (2017). <https://doi.org/10.1016/j.materresbull.2017.04.013>.
 - Y.J. Wong, J. Hassan, and M. Hashim, Dielectric properties, impedance analysis and modulus behavior of CaTiO_3 ceramic prepared by solid state reaction. *J. Alloy. Compd.* 571, 138–144 (2013). <https://doi.org/10.1016/j.jallcom.2013.03.123>.

32. P. Kamkum, N. Atiwongsangthong, R. Muanghlua, and N. Vittayakorn, Application of chicken eggshell waste as a starting material for synthesizing calcium niobate ($\text{Ca}_4\text{Nb}_2\text{O}_9$) powder. *Ceram. Int.* 41, S69–S75 (2015). <https://doi.org/10.1016/j.ceramint.2015.03.189>.
33. S. Chaudhary, S. Devi, and S. Jindal, Enhancing structural, optical, magnetic, dielectric and impedance properties of $\text{Ba}_{0.95}\text{Sr}_{0.05}\text{Ca}_5\text{Ti}_{2-x}\text{Fe}_x\text{Nb}_8\text{O}_{30}$ tungsten bronze ferroelectric ceramic through Fe/Ti ratio on optimization for the advanced device applications. *Mater. Chem. Phys.* 312, 128580 (2024). <https://doi.org/10.1016/j.matchemphys.2023.128580>.
34. L. Malik, G.S. Saini, and A. Tevatia, A self-sustained machine learning model to predict the in-flight mechanical properties of a rocket nozzle by inputting material properties and environmental conditions, *Handbook of Sustainable Materials: Modelling, Characterization, and Optimization*. (Boca Raton: CRC Press, 2023), pp. 431–456. <https://doi.org/10.1201/9781003297772>.
35. L. Malik, S. Rawat, M. Kumar, and A. Tevatia, Simulation studies on aerodynamic features of Eurofighter Typhoon and Dassault Rafale combat aircraft. *Mater. Today: Proc.* 38, 191–197 (2021). <https://doi.org/10.1016/j.matpr.2020.06.536>.
36. L. Malik, G.S. Saini, M. Malik, and A. Tevatia, Sustainability of wind turbine blade: instantaneous real-time prediction of its failure using machine learning and solution based on materials and design, *Handbook of Sustainable Materials: Modelling, Characterization, and Optimization*. (Boca Raton: CRC Press, 2023), pp. 399–430. <https://doi.org/10.1201/9781003297772>.
37. L. Malik and A. Tevatia, Comparative analysis of aerodynamic characteristics of F16 and F22 combat aircraft using computational fluid dynamics. *Def. Sci. J.* 71, 137–145 (2021). <https://doi.org/10.14429/dsj.71.15762>.
38. L. Malik, Novel concept of tailorable magnetic field and electron pressure distribution in a magnetic nozzle for effective space propulsion. *Propul. Power Res.* 12, 59–68 (2023). <https://doi.org/10.1016/j.jprr.2023.02.002>.
39. L. Malik, In-flight plume control and thrust tuning in magnetic nozzle using tapered-coils system under the effect of density gradient. *IEEE Trans. Plasma Sci.* 51, 1325–1333 (2023).

Publisher's Note Springer Nature remains neutral with regard to jurisdictional claims in published maps and institutional affiliations.

Springer Nature or its licensor (e.g. a society or other partner) holds exclusive rights to this article under a publishing agreement with the author(s) or other rightsholder(s); author self-archiving of the accepted manuscript version of this article is solely governed by the terms of such publishing agreement and applicable law.